Composite Structures 132 (2015) 1043–1055

Contents lists available at ScienceDirect

Composite Structures

journal homepage: www.elsevier.com/locate/compstruct

An experimental investigation of interlaminar and intralaminar dynamic fracture of CFRPs: Effect of matrix modification using carbon nanotubes

Robert W. Bedsole [a], Philip B. Bogert [b], Hareesh V. Tippur [a,*]

[a] Department of Mechanical Engineering, Auburn University, AL 36849, United States
[b] Structural Mechanics and Concepts, NASA-LaRC, Hampton, VA 23681-2199, United States

ARTICLE INFO

Article history:
Available online 14 July 2015

Keywords:
Dynamic fracture
Inter-/Intra-laminar fracture
Carbon fiber reinforced composites
Digital image correlation
Carbon nanotubes
Ultrasonic measurements

ABSTRACT

In this work, mode-I dynamic interlaminar and intralaminar fracture behaviors of carbon fiber reinforced polymers (CFRPs) are studied. Thick unidirectional composites were fabricated and their fracture performance was characterized under quasi-static three-point bending and dynamic one-point impact loading conditions. Both crack initiation and growth characteristics under stress-wave dominant conditions were evaluated in the latter case. The optical methods of digital image correlation (DIC) and ultra-high speed photography were employed to monitor crack tip deformations around transiently growing cracks. All relevant elastic properties were measured ultrasonically in order to determine stress intensity factors (SIFs). Interlaminar fracture responses were compared to the intralaminar counterparts using specimens of identical dimensions from the same original composite plate. Carbon nanotubes (CNTs) were then added with the aim of improving interlaminar fracture properties. While CNTs did not lead to improvements in critical stress intensity factor (K_{IC}/K^d_{I-ini}), they did lead to modest improvements in fracture toughness (G_{IC}/G^d_{I-ini}) under both quasi-static (+34%) and dynamic (+16%) loading conditions with significant scatter observed in these measurements.

1. Introduction

In recent years carbon fiber reinforced polymers (CFRPs) have become a mainstay of aerospace structures. These layered systems are susceptible to fracture/damage in the interlaminar regions, particularly as a result of fatigue and/or impact loading; however, interlaminar fracture of composites is more tedious to characterize than intralaminar fracture. For a unidirectional composite, these two types of fracture are ideally very similar. Therefore, several authors [1–4] have compared intralaminar and interlaminar crack growth of unidirectional CFRPs under quasi-static loading conditions; however, to the authors' knowledge, none have used the same specimen geometry when comparing intralaminar and interlaminar specimens. Most [1,2,4] used double cantilever beam (DCB) specimens to examine interlaminar fracture and compact tension specimens to examine intralaminar fracture, whereas de Moura et al. [3] used DCB specimens of different geometries to examine interlaminar and intralaminar fracture. Because measured stress intensity factors (SIFs) are dependent on specimen geometry [5–7], the present work involves the fabrication of thick carbon fiber composites such that both interlaminar and intralaminar specimens with the same geometry can be prepared from the same sheet and tested under similar conditions.

In order to reinforce the relatively weak interlaminar regions of CFRPs, several investigatiors [8–16] have added carbon nanotubes (CNTs) to this region. All used a DCB specimen to measure critical energy release rate (G_{IC}) under quasi-static loading conditions (typically following the ASTM Standard D5528 [8–10,12–16]). Some of the authors [9,10,13,15,16] formed their three-phase nanocomposites by dispersing CNTs into the resin first (Table 1), while others [8,11,12,14] began with carbon fiber sheets pre-impregnated with resin and then added CNTs by a sifting or spraying technique (Table 2). Most [8,11,12] of the latter group added CNTs only to the interlayer where the pre-crack would be introduced. Note that SWCNTs, DWCNTs, and MWCNTs refer to single-walled, double-walled, and multi-walled CNTs, respectively, whereas "UF" refers to unfunctionalized CNTs. In the current work, CNTs are incorporated first into the resin, and then the CNT/resin mixture is painted between layers of carbon fiber using a hand layup procedure similar to the methodology of Karapappas et al. [13] and Romhany and Szebenyi. [15]

Finally, the study of high loading-rate fracture in composites is critical for materials that will be used in aerospace applications

* Corresponding author. Tel.: +1 334 844 3327.
E-mail address: tippuhv@auburn.edu (H.V. Tippur).

http://dx.doi.org/10.1016/j.compstruct.2015.07.016
0263-8223/

Table 1
Reported fracture toughness (G_{IC}) of carbon fiber nanocomposites with CNTs dispersed into the resin first.

Author	+% G_{IC}	Fiber Layout (manufacturing technique)	Fiber V_f%	CNT type (dispersion technique)
Ashrafi et al. [9]	3[a]	$[0°]_n$ fabric (prepreg with CNTs)[b]	–	0.1 wt% SWCNTs (bath sonication + solvent)
Godara et al. [10]	40	$[0°]_n$ fabric (prepreg with CNTs)[b]	50–60	0.5 wt% NH_2 DWCNTs (calendering)
Karapappas et al. [13]	60	$[0°]_n$ fabric (hand layup)	56	1 wt% UF MWCNTs (high shear mill)
Romhany and Szebenyi [15]	13[a]	$[0°]_n$ fabric (hand layup)	52	0.3 wt% UF MWCNTs (calendering)
Sager et al.[c] [16]	18[a]	Woven fabric (VARTM + interleaf film)	55	0.5 wt% NH_2 CNTs (bath sonication + solvent)

[a] Indicates % improvement that was not significant relative to the reported error bars.
[b] Prepreg in this table indicates that CNTs were dispersed into the resin before the impregnation of dry fibers.
[c] Used the same epoxy system as the current work.

Table 2
Reported fracture toughness (G_{IC}) of carbon fiber nanocomposites with CNTs added last to epoxy/carbon fiber prepreg.

Author	+% G_{IC}	Fiber Layout (manufacturing technique)	Fiber V_f%	CNT Type (dispersion technique)
Almuhammadi et al. [8]	17	$[0°]_n$ prepreg[b] (CNTs sprayed on)	57	0.5 wt% COOH MWCNTs (sonication + solvent)
Hu et al. [11]	58	$[0°]_n$ prepreg[b] (CNTs sifted onto interlayer)	–	10 g/m^2 UF MWCNTs
Joshi and Dikshit [12]	40	Woven prepreg[b] (CNTs sprayed on)	67	1.32 g/m^2 UF MWCNTs (bath sonication + solvent)
Kim and Hahn [14]	6	$[0°]_n$ prepreg[b] (CNTs sprayed on)	65	0.5 wt% COOH SWCNTs (bath sonication + solvent)

[a] All % improvements in this table were significant relative to the error bars.
[b] Prepreg in this table indicates that CNTs were added to carbon fibers that had been previously impregnated with resin.

where cold temperatures and high speeds typically elicit a more brittle response. Therefore, a few previous works [17–20] have employed strain gages in order to evaluate dynamic fracture parameters of interlaminar cracks in unidirectional CFRP samples. Instead of strain gages, the present work is the first to use digital image correlation (DIC) to map full-field deformations before and after crack initiation in order to determine interlaminar SIF histories in fiber-reinforced composite specimens subjected to dynamic impact loading. The advantage of using optical methods is that, unlike strain gages, they provide non-contact full-field deformations, as well as the precise location of the crack tip during the fracture event, which is necessary for estimating crack tip velocities for an accurate evaluation of dynamic SIF histories and hence crack growth resistance. This is particularly important because different CFRP systems could have different post-initiation resistance behaviors [21], an important factor in material selection.

In this context, it should be emphasized that energy release rate (G) is more relevant in characterizing fracture behavior of CFRPs. Further, direct evaluation of G without first finding SIFs is feasible under quasi-static conditions, as far-field load–displacement measurements are readily relatable to the crack tip stresses and displacements. However, the same is not true for stress-wave dominant conditions involving dynamic crack initiation and high-speed crack growth. That is, the far-field and near field quantities are not readily relatable as they temporally evolve during dynamic events such as shock and impact loading. Therefore, crack tip mechanical field (displacements and stresses) measurements to determine SIFs, followed by subsequent evaluation of G using elastic properties of the composite, is a possible approach when direct full-field crack tip measurements are performed.

In light of this, all relevant in-plane and out-of-plane elastic properties necessary to evaluate both inter- and intralaminar SIFs are determined ultrasonically for each material system as part of the experimental program undertaken. This aspect is also unique to the reported dynamic fracture data as many other authors [18–21] adopted statically measured properties to estimate dynamic fracture parameters and/or relied on material characteristics of similar materials reported by others to accomplish the task. These authors [18–21] also used in-plane characteristics to estimate out-of-plane properties by assuming transverse isotropy.

In the present work, carbon nanotubes have been introduced into the interlaminar region of unidirectional CFRP specimens with the goal of enhancing interlaminar and intralaminar fracture properties under quasi-static and dynamic loading conditions. In order to achieve identical geometry between interlaminar and intralaminar fracture specimens, as well as to minimize the effects of wave reflections during dynamic fracture tests, sufficiently thick CFRP specimens have been fabricated. A methodology based on DIC has been developed to study dynamic interlaminar crack initiation and growth in a fiber-reinforced composite material subjected to dynamic loading. The SIF histories before *and* after crack initiation have been generated using displacement fields (determined by DIC) along with the ultrasonically-determined elastic properties.

2. Specimen preparation

Unidirectional carbon fiber fabric was provided by V2 Composites, Inc. The resin system was Epon 862 and curing agent Epikure W from Momentive Specialty Chemicals, Inc. Two thick CFRPs were prepared in order to compare the effects of carbon nanotubes on the interlaminar and intralaminar fracture properties: carbon fiber/epoxy (“Neat”) and CNT/carbon fiber/epoxy (with multi-walled NH_2-functionalized NC 3152 CNTs from Nanocyl, <1 μm length, 9.5 nm diameter). CNTs were dispersed by calendering with a masterbatch technique using an Exakt 80E Calender. CNTs were first dispersed in the resin at 1.3 wt% using the calender until a thick paste was formed. This masterbatch was diluted with additional resin to 0.4 wt% CNTs by hand-stirring, followed by additional passes through the calender. Lastly, Epikure W was hand-stirred and mechanically stirred in, such that the final weight percentage of CNTs in epoxy was 0.3 wt%. Scanning electron microscopy of fracture surfaces of CNT/epoxy nanocomposites reported elsewhere [22] indicates good dispersion of CNTs by this method (Fig. 1a).

Thick CFRP plates were fabricated using a hand layup and vacuum-bagging procedure. Resin (with or without pre-dispersed CNTs) was painted on between each of 60 layers of unidirectional carbon fiber fabric (held together by a scrim material as shown in Fig. 2), all oriented in the same direction ($[0°]_{60}$) (Fig. 3a). Each sample was originally cured for 2.5 h at 120 °C inside a vacuum bag. Samples were then machined with a tile saw to create interlaminar and intralaminar specimens from the same original composite plate; interlaminar and intralaminar orientations are given schematically in Fig. 3b. Dimensions of interlaminar slices are

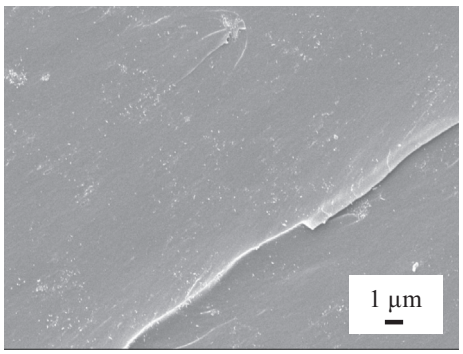

Fig. 1. Scanning electron micrograph of a fracture surface of an NH_2–CNT/epoxy nanocomposite showing good dispersion of CNTs.

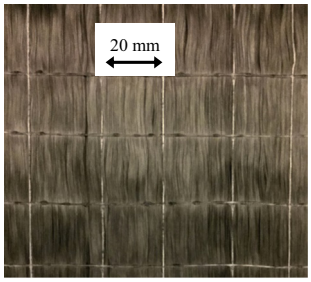

Fig. 2. 0/90 scrim material (white) on the front and back surfaces of unidirectional carbon fiber fabric. Carbon fibers are running vertically.

given in Fig. 4a. Three such interlaminar slices were stacked and glued together (Fig. 4b) in a vise using the same epoxy system as before in order to achieve ~50 mm thick interlaminar samples. Both interlaminar and intralaminar specimens were heated back to 120 °C for 2.5 h (in order to cure the epoxy glue used in interlaminar specimens) before post-curing for 3 h at 180 °C, such that the final geometry of all interlaminar and intralaminar fracture specimens were identical (Fig. 5), and all samples were subjected to identical curing schedules. Specimens were given a speckle coating for performing measurements using DIC. Pre-notches were then made with a diamond-tipped saw and sharpened by pressing a razor blade into the notch tip. This notching technique was chosen as an alternative to the difficulties of Teflon tape insertion for intralaminar samples detailed in Czabaj and Ratcliffe [2], who also measured interlaminar and intralaminar fracture of specimens machined from the same original composite sheet.

3. Experimental details

3.1. Quasi-static fracture test setup

Three-point bend quasi-static fracture tests (Fig. 6a) were performed on an Instron 4465 test stand at a crosshead speed of 0.01 mm/s using a 5 kN load cell. Load-point displacement was assumed to be the crosshead displacement. Load and displacement data were collected at a sample rate of 10 s^{-1}. Digital images were recorded every 3 s for determining SIFs from surface displacement fields. The critical SIF (K_{IC}) was chosen to be the SIF associated with the image immediately prior to visible crack tip movement. Crack growth was continued at least until the load decreased below half

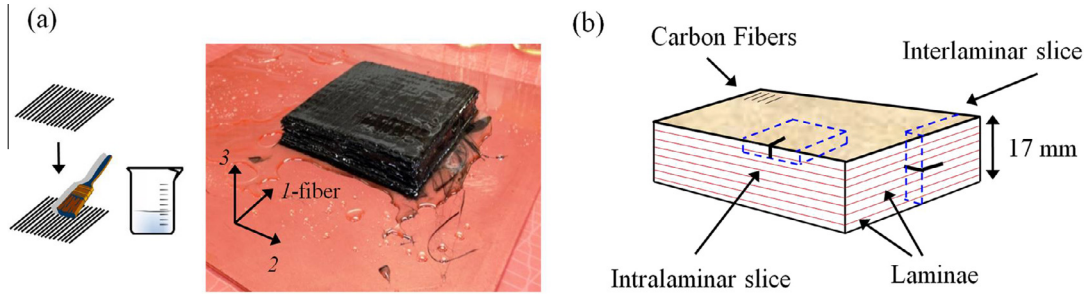

Fig. 3. CFRP plate preparation details: (a) wet layup procedure for 60-layer CFRPs. (b) Orientation of interlaminar and intralaminar slices machined from the same thick composite plate.

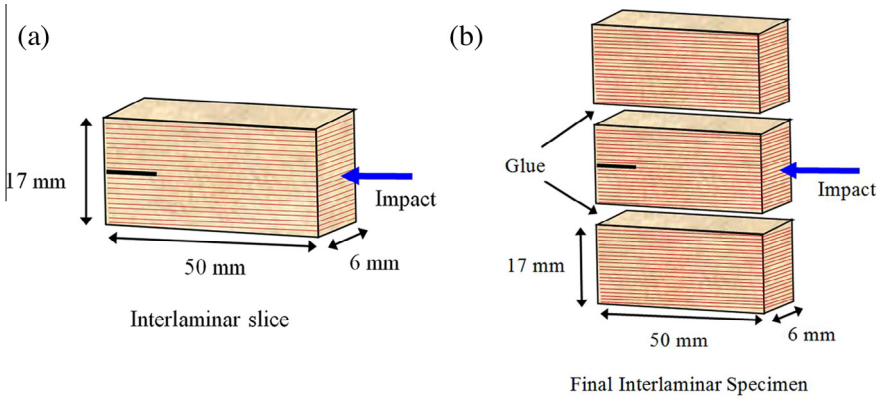

Fig. 4. Interlaminar specimen preparation details: (a) Dimensions of a single interlaminar slice machined from the CFRP manufactured in Fig. 3 for dynamic fracture experiments. (b) Preparation of dynamic interlaminar fracture specimens by stacking and gluing three blocks with the dimensions shown in (a).

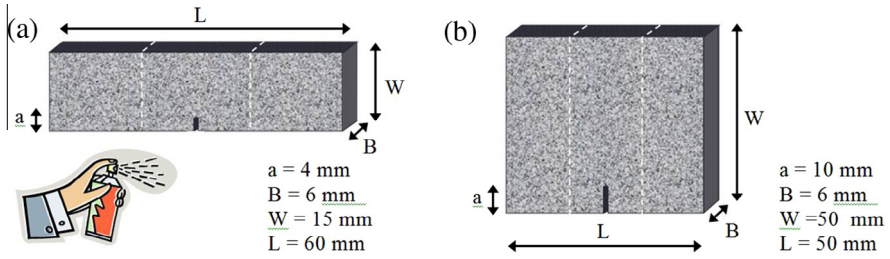

Fig. 5. Dimensions of fracture specimens subjected to (a) quasi-static loading and (b) dynamic impact loading. White dash lines indicate epoxy glue lines for interlaminar specimens. All specimens were given a speckle coating for performing DIC.

of the peak load, at which time cracks had all grown well beyond an a/W value of 0.5.

3.2. Dynamic fracture test setup

Dynamic 1-point impact tests were performed using a Hopkinson pressure bar (long-bar), depicted in Fig. 6b. Compressed air was used to launch a striker (25.4 mm diameter, 0.30 m length) coaxially towards the long-bar (25.4 mm diameter, 1.83 m length) of the same material (strain-rate independent aluminum 7075 T6). A soft aluminum pulse shaper was used between the striker and the long-bar to temper the loading rate such that more images could be captured in the pre- and post-initiation phases of the dynamic fracture event. The long-bar has a semi-circular (cylindrical) head machined on the end initially in contact with the specimen in order to deliver thickness-wise line-loading (1-point impact) to the specimen. The compressive stress wave traveled across the specimen, reached the free edge with the pre-notch, reflected back as a tensile wave, opened the pre-notch, initiated crack growth, and drove the crack to velocities as high as 800 m/s, all while inertia was holding the specimen within the view of the ultra-high speed camera. A roller of putty was placed above and below the specimen for the purpose of specimen alignment and in order to ensure symmetric wave reflections from the top and bottom surfaces of the specimen under "free-free" conditions. A Cordin ultra-high speed camera collected 32 digital images during the fracture event at 300,000 frames per second. A strain gage on the long-bar was used to collect stress wave data for independent estimation of SIFs prior to crack initiation using finite element analysis (FEA) software (see Section 3.5).

3.3. Experimental analysis

In both quasi-static and dynamic fracture experiments, undeformed images (recorded prior to loading) were paired with deformed images, and the resulting displacement fields were determined using ARAMIS image analysis software (DIC). Recorded 1000 by 1000 pixel images were divided into 15 by 15 pixel non-overlapping subimages (Fig. 7a), resulting in ~60 by 60 data points of displacement for each pair of images. (All images have been flipped in order to comply with standard linear elastic fracture mechanics notation with origin at the crack tip and the crack growing in the positive x-direction.) The location of the center of each subimage was tracked, and corresponding opening (v) and sliding (u) displacements were measured relative to their original positions in the undeformed images (Fig. 7b).

Sample digital images from an interlaminar dynamic fracture test of neat epoxy/carbon fiber are given in Fig. 8a, along with corresponding v-displacement fields (Fig. 8b) and u-displacement fields (Fig. 8c) determined by DIC. Notice that there are no discontinuities in the displacements where interlaminar specimens were glued together. Displacement data from the area behind the crack tip (where opening displacements are significant) in the range $0.5 < r/B < 1.5$, where r is the radial distance of the polar coordinate system (r,θ) with origin at the crack tip, is used to determine SIFs in order to avoid three-dimensional (3-D) effects near the crack tip.

The following orthotropic displacement field equations [23] are used to determine SIFs for each deformed image for all quasi-static specimens, as well as for all dynamic specimens prior to crack initiation:

$$u(r,\theta) = K_I\sqrt{\frac{2r}{\pi}}\mathrm{Re}\left[\frac{1}{\mu_2-\mu_1}(p_1\mu_2 z_1 - p_2\mu_1 z_2)\right] + K_{II}\sqrt{\frac{2r}{\pi}}\mathrm{Re}\left[\frac{1}{\mu_2-\mu_1}(p_1 z_1 - p_2 z_2)\right]$$

$$v(r,\theta) = K_I\sqrt{\frac{2r}{\pi}}\mathrm{Re}\left[\frac{1}{\mu_2-\mu_1}(q_1\mu_2 z_1 - q_2\mu_1 z_2)\right] + K_{II}\sqrt{\frac{2r}{\pi}}\mathrm{Re}\left[\frac{1}{\mu_2-\mu_1}(q_1 z_1 - q_2 z_2)\right]. \quad (1)$$

For intralaminar fracture of an orthotropic material with x–z and y–z planes as symmetry planes: $\mu_j\,(j=1,2)$ are the two roots of: $S_{11}\mu^4 + (2S_{12}+S_{66})\mu^2 + S_{22} = 0$,

$$p_j = \mu_j^2 S_{11} + S_{12},\quad q_j = \mu_j S_{12} + \frac{S_{22}}{\mu_j},\quad z_j = \sqrt{\cos\theta + \mu_j \sin\theta},$$

$$\begin{pmatrix}\varepsilon_{11}\\ \varepsilon_{22}\\ \varepsilon_{33}\\ 2\varepsilon_{23}\\ 2\varepsilon_{31}\\ 2\varepsilon_{12}\end{pmatrix} = \begin{pmatrix} S_{11} & S_{12} & S_{13} & 0 & 0 & 0\\ S_{21} & S_{22} & S_{23} & 0 & 0 & 0\\ S_{31} & S_{32} & S_{33} & 0 & 0 & 0\\ 0 & 0 & 0 & S_{44} & 0 & 0\\ 0 & 0 & 0 & 0 & S_{55} & 0\\ 0 & 0 & 0 & 0 & 0 & S_{66}\end{pmatrix}$$

$$= \begin{pmatrix} \frac{1}{E_1} & \frac{-\upsilon_{21}}{E_2} & \frac{-\upsilon_{31}}{E_3} & & & \\ \frac{-\upsilon_{12}}{E_1} & \frac{1}{E_2} & \frac{-\upsilon_{32}}{E_3} & 0 & 0 & 0\\ \frac{-\upsilon_{13}}{E_1} & \frac{-\upsilon_{23}}{E_2} & \frac{1}{E_3} & & & \\ 0 & 0 & 0 & \frac{1}{G_{23}} & 0 & 0\\ 0 & 0 & 0 & 0 & \frac{1}{G_{31}} & 0\\ 0 & 0 & 0 & 0 & 0 & \frac{1}{G_{12}}\end{pmatrix}\begin{pmatrix}\sigma_{11}\\ \sigma_{22}\\ \sigma_{33}\\ \sigma_{23}\\ \sigma_{31}\\ \sigma_{12}\end{pmatrix}. \quad (2)$$

Equation (2) can be readily modified for the case of *interlaminar* fracture of an orthotropic material with x–z and y–z planes as symmetry planes, where S_{13}, S_{33}, and S_{55} are used instead of S_{12}, S_{22}, and S_{66}, respectively.

In the above equations, K_I is the mode-I SIF, K_{II} is the mode-II SIF (which is expected to be near zero for this symmetric loading case), and u and v are the sliding and opening displacements. A least-squares analysis was used to determine a single K_I and K_{II} value for each pair of images. For consistency, the critical SIF (K_{IC} for quasi-static loading and K^d_{I-ini} for dynamic loading) was chosen to be the mode-I SIF value for the image immediately prior to visible crack initiation in the images. The S-matrix in Eq. (2) relates stresses and strains for an orthotropic material. Details of the

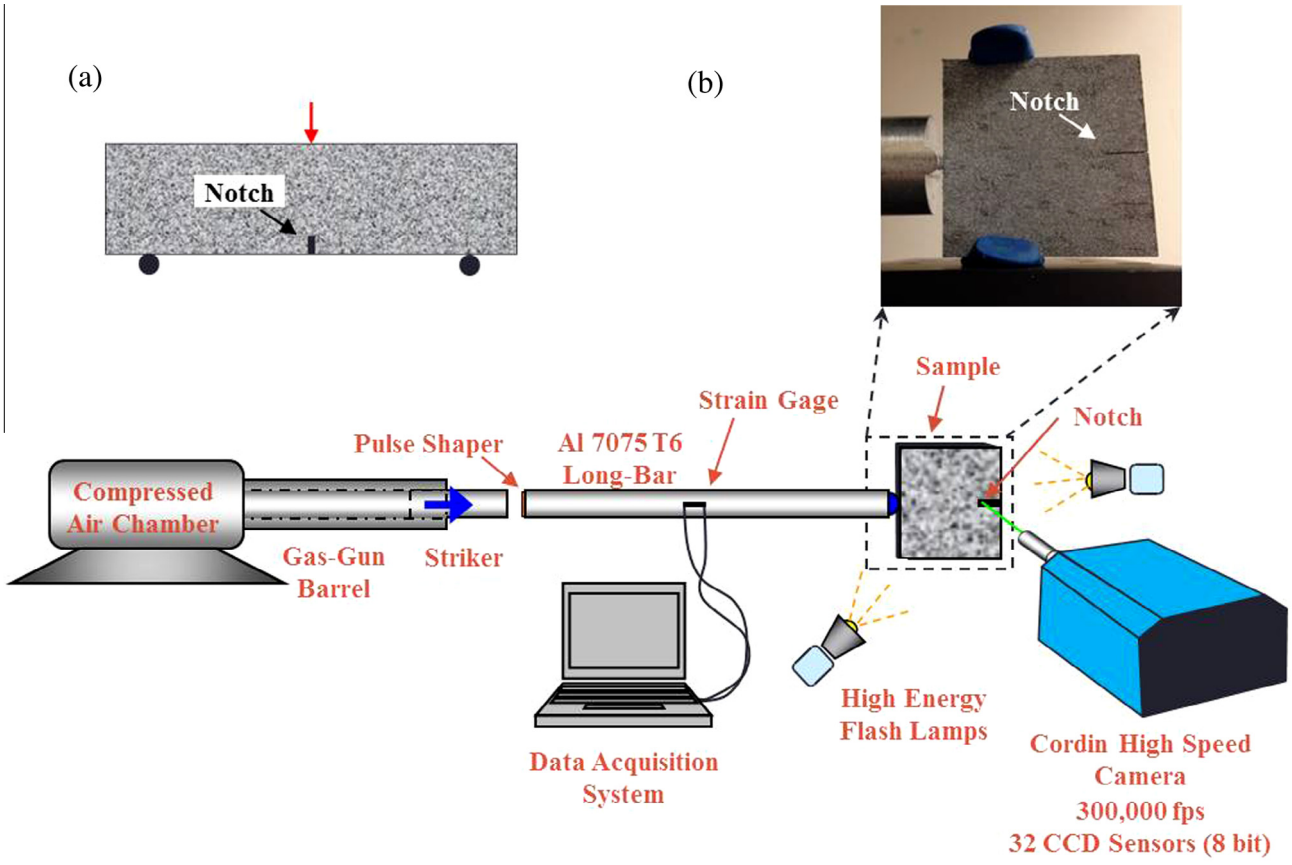

Fig. 6. Specimen and experimental setup details: (a) quasi-static 3-point bending of edge-cracked specimen and (b) dynamic 1-point impact of edge-cracked specimen.

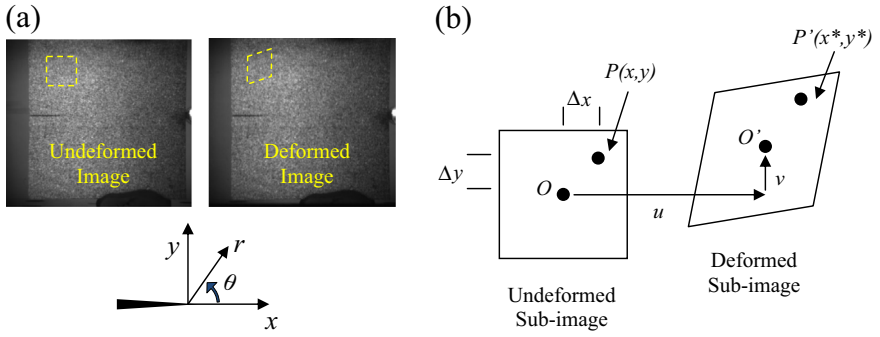

Fig. 7. Working principle of 2D DIC: (a) sub-images are identified in undeformed images, and the corresponding deformed subimages are located in the deformed image. (b) u and v displacements are assigned to each subimage. Speckle size is 4–6 pixels/speckle. Scale factor is 50 μm/pixel.

ultrasonic method for determining these elastic orthotropic material properties are given in Section 3.4. For the case of a dynamically growing crack, the orthotropic displacement field equations [24] are:

$$u(r,\theta)=\frac{2}{C_{66}R(c)}\mathrm{Re}\left[\left(\frac{\mu_2-\lambda_2}{\lambda_1-\lambda_2}\sqrt{\frac{z_1}{2\pi}}-\frac{\mu_1-\lambda_1}{\lambda_1-\lambda_2}\sqrt{\frac{z_2}{2\pi}}\right)K_I^d-\left(\frac{\gamma-\lambda\eta^2\mu_2\lambda_2}{\lambda_1-\lambda_2}\sqrt{\frac{z_1}{2\pi}}-\frac{\gamma-\lambda\eta^2\mu_1\lambda_1}{\lambda_1-\lambda_2}\sqrt{\frac{z_2}{2\pi}}\right)K_{II}^d\right]$$

$$v(r,\theta)=\frac{2}{C_{66}R(c)}\mathrm{Re}\left[-\left(\lambda_1\frac{\mu_2-\lambda_2}{\lambda_1-\lambda_2}\sqrt{\frac{z_1}{2\pi}}-\lambda_2\frac{\mu_1-\lambda_1}{\lambda_1-\lambda_2}\sqrt{\frac{z_2}{2\pi}}\right)K_I^d+\left(\lambda_1\frac{\gamma-\lambda\eta^2\mu_2\lambda_2}{\lambda_1-\lambda_2}\sqrt{\frac{z_1}{2\pi}}-\lambda_2\frac{\gamma-\lambda\eta^2\mu_1\lambda_1}{\lambda_1-\lambda_2}\sqrt{\frac{z_2}{2\pi}}\right)K_{II}^d\right]. \quad (3)$$

For *intralaminar* fracture of an orthotropic material with x–z and y–z planes as symmetry planes, $\mu_j\,(j=1,2)$ are the 2 roots of: $\mu^4+\left(\alpha_l^2(c)\eta^2+\frac{\alpha_s^2(c)}{\eta^2\lambda}-\frac{(1+\gamma)^2}{\eta^2\lambda}\right)\mu^2+\frac{\alpha_l^2(c)\alpha_s^2(c)}{\lambda}=0$,

$$\lambda=\frac{S_{11}}{S_{22}},\quad \zeta=\frac{2S_{12}+S_{66}}{2\sqrt{S_{11}S_{22}}},\quad \kappa=\frac{3\sqrt{S_{11}S_{22}}+S_{12}}{\sqrt{S_{11}S_{22}}-S_{12}},\quad c_l=\sqrt{\frac{C_{11}}{\rho}},$$

$$c_s=\sqrt{\frac{C_{66}}{\rho}},\quad \alpha_l^2(c)=1-\left(\frac{c}{c_l}\right)^2,\quad \alpha_s^2(c)=1-\left(\frac{c}{c_s}\right)^2,$$

$$\eta^2=\left(\frac{\kappa+1}{\kappa-1}\right)\left(\frac{3-\kappa+\zeta(\kappa+1)}{4\sqrt{\lambda}}\right),\quad \gamma=\sqrt{\lambda}\eta^2\left(\frac{3-\kappa}{1+\kappa}\right),$$

$$\lambda_j(c)=\frac{\eta^2\alpha_l^2(c)+\mu_j^2(c)}{(1+\gamma)\mu_j(c)}\quad (j=1,2),$$

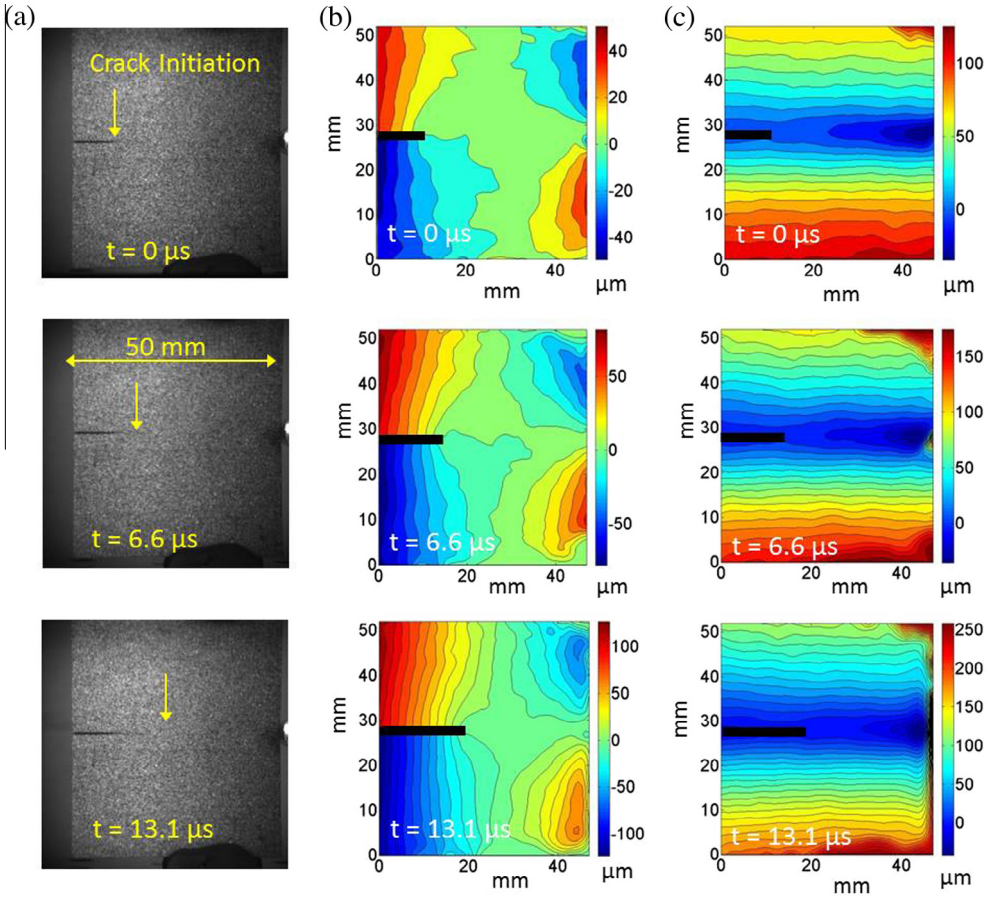

Fig. 8. (a) Three of 32 images from an interlaminar dynamic fracture test of neat epoxy/carbon fiber (arrows indicate the approximate location of the crack tip), (b) v-opening contours of displacement, and (c) u-sliding contours of displacement. The crack initiates at time $t = 0$. Contour interval is 10 μm.

$$R(c) = \sqrt{\lambda}\eta^2\alpha_l(c)\alpha_s(c) - \frac{\sqrt{\lambda}\eta^2\alpha_l(c) + \gamma^2\alpha_s(c)}{\sqrt{\lambda}\eta^2\alpha_l(c) + \alpha_s(c)}, \quad z_j = r(\cos\theta + \mu_j \sin\theta). \tag{4}$$

Again, for *interlaminar* fracture of an orthotropic material with x–z and y–z planes as symmetry planes, S_{13}, S_{33}, S_{55}, and C_{55} are used instead of S_{12}, S_{22}, S_{66}, and C_{66}, respectively, in Eq. (4).

In Eqs. (3) and (4), K_I^d and K_{II}^d are the mode-I and mode-II SIFs for a dynamically growing crack tip, c is the crack tip velocity, ρ is the mass density, and C_{11} and C_{66} are elements of the stiffness (C) matrix, which is the inverse of the S-matrix given in Eq. (2):

$$\begin{pmatrix} \sigma_{11} \\ \sigma_{22} \\ \sigma_{33} \\ \sigma_{23} \\ \sigma_{31} \\ \sigma_{12} \end{pmatrix} = \begin{pmatrix} C_{11} & C_{12} & C_{13} & 0 & 0 & 0 \\ C_{21} & C_{22} & C_{23} & 0 & 0 & 0 \\ C_{31} & C_{32} & C_{33} & 0 & 0 & 0 \\ 0 & 0 & 0 & C_{44} & 0 & 0 \\ 0 & 0 & 0 & 0 & C_{55} & 0 \\ 0 & 0 & 0 & 0 & 0 & C_{66} \end{pmatrix} \begin{pmatrix} \varepsilon_{11} \\ \varepsilon_{22} \\ \varepsilon_{33} \\ 2\varepsilon_{23} \\ 2\varepsilon_{31} \\ 2\varepsilon_{12} \end{pmatrix}, \quad [C] = [S]^{-1}. \tag{5}$$

3.4. Ultrasonic determination of elastic constants

Because the primary emphasis of this work is dynamic fracture, ultrasonic determination of material properties is more appropriate than the quasi-static measurements typically reported in the literature. Several authors [25,26] have measured the elastic constants of composite materials; however, this will be the first work to measure the constants ultrasonically in both in-plane and out-of-plane directions for fracture parameter assessment.

The coefficients of the C-matrix were determined using an Epoch 600 Ultrasonic Flaw Detector from OLYMPUS in through-transmission mode. Composite material cubes were machined such that the faces aligned with the 1-, 2-, and 3-directions (Fig. 9), as defined originally in Fig. 3, where 1 – is the fiber and crack growth direction, 2 – is the crack opening direction for intralaminar specimens, and 3 – is the crack opening direction for interlaminar specimens.

Following the notations used in [27], let V_{ij} denote the speed of a wave traveling in the i-direction with displacements in the j-direction. V_{11}, V_{22}, and V_{33} are then longitudinal wave speeds, whereas V_{12}, V_{13}, and V_{23} are shear wave speeds. These wave speeds are related to the diagonal terms of the C-matrix according to the following equations, where ρ is mass density:

$$\begin{aligned} C_{11} &= \rho V_{11}^2, \quad C_{44} = \rho V_{23}^2 = \rho V_{32}^2, \\ C_{22} &= \rho V_{22}^2, \quad C_{55} = \rho V_{13}^2 = \rho V_{31}^2, \\ C_{33} &= \rho V_{33}^2, \quad C_{66} = \rho V_{12}^2 = \rho V_{21}^2. \end{aligned} \tag{6}$$

In order to measure the off-diagonal terms of the C-matrix, three additional cubes were machined as before, and then parallel slices were taken with a 45° angle relative to the 1-, 2-, or 3-directions. A 45° rotation about the *1*-direction is shown in Fig. 10 with slices taken between the 2- and 3-faces. This new face is labeled the "6-face," with corresponding longitudinal wave speed denoted as V_{66}.[1] Similarly, V_{44} was measured using opposing faces between the 1- and 2-faces, whereas V_{55} was measured using opposing faces

[1] For simplicity, the notation for wave speeds V_{44}, V_{55}, and V_{66}, differs from [27].

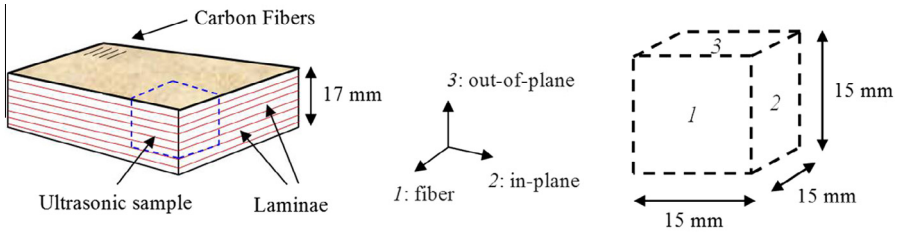

Fig. 9. Orientation of cube specimens for ultrasonic determination of orthotropic elastic constants.

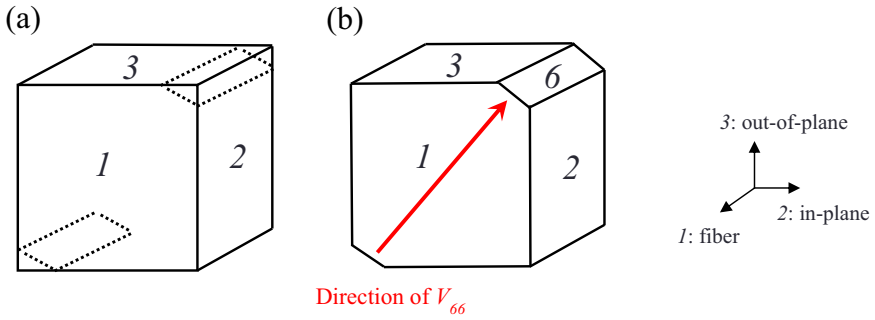

Fig. 10. In order to measure V_{66}, (a) an original cube like the one in Fig. 9 is machined. (b) Opposite corners are milled off between the 2- and 3-faces, such that ultrasonic transducer and receiver can be placed on the newly milled faces.

between the 1- and 3-faces. The off-diagonal C-matrix terms are then given by [27]:

$$C_{12} = C_{21} = \sqrt{(C_{11} + C_{66} - 2\rho V_{44}^2)(C_{22} + C_{66} - 2\rho V_{44}^2)} - C_{66},$$
$$C_{13} = C_{31} = \sqrt{(C_{11} + C_{55} - 2\rho V_{55}^2)(C_{33} + C_{55} - 2\rho V_{55}^2)} - C_{55}, \quad (7)$$
$$C_{23} = C_{32} = \sqrt{(C_{22} + C_{44} - 2\rho V_{66}^2)(C_{33} + C_{44} - 2\rho V_{66}^2)} - C_{44}.$$

Once all 12 nonzero terms of the C-matrix coefficients are determined, the C-matrix (Eq. (5)) can be inverted in order to obtain the S-matrix (Eq. (2)). The resulting material properties are listed in Table 3, where "Neat" refers to epoxy/carbon fiber composites and "CNT" refers to CNT/epoxy/carbon fiber nanocomposites. The C-matrix coefficients are also compared to those given by Solodov et al. [26], who measured all 9 independent elastic constants ultrasonically for a nearly unidirectional carbon fiber composite (18 aligned 0° plies with 2 ± 45° plies in the center). Neat CFRP values follow the same trends as those found in the literature [26] at a slightly lower magnitude. This decrease in magnitudes may be due to a lower density of the material processed for this work. Additional application of this methodology to cortical bone is reported in Appendix A, where measured values performed by this methodology on bovine cortical bone closely matched those found in the literature (Table A1), further supporting the reported measurements.

Table 3
Material properties of thick CFRPs ('Neat' refers to epoxy/carbon fiber composites. 'CNT' refers to CNT/epoxy/carbon fiber nanocomposites).

Material property	Neat	CNT	C-matrix coefficient	Neat	Literature [26]
E_1 (GPa)	94.54	100.72	C_{11} (GPa)	102	127
E_2 (GPa)	8.29	7.60	C_{22} (GPa)	11.6	13.8
E_3 (GPa)	7.10	4.34	C_{33} (GPa)	10.0	12.8
G_{23} (GPa)	2.47	2.00	C_{44} (GPa)	2.5	3.6
G_{13} (GPa)	4.32	3.67	C_{55} (GPa)	4.3	5.0
G_{12} (GPa)	5.31	5.11	C_{66} (GPa)	5.3	6.7
υ_{12}	0.42	0.41	C_{12} (GPa)	8	7
υ_{13}	0.52	0.54	C_{13} (GPa)	8	6
υ_{23}	0.54	0.58	C_{23} (GPa)	6	7
υ_{21}	0.04	0.03	ρ (kg/m^3)	1482	1600
υ_{31}	0.04	0.02			
υ_{32}	0.46	0.33			
Fiber V_f	50%	44%			
ρ (kg/m^3)	1482	1442			

From the above table, a slight drop in the material density with the inclusion of CNTs into the matrix is evident. This is attributed to increased viscosity of CNT-modified resin, which caused less resin to be vacuumed out during curing. This contributed to modestly higher resin content, causing a decrease in ρ, E_2, E_3, G_{12}, G_{13}, and fiber volume fraction V_f. By intentionally manipulating the elastic constant input while solving Eqs. (1)–(4), it was found that the shear moduli (G_{12},G_{13}) have the greatest effect on measured SIFs, whereas crack-opening direction elastic moduli (E_2,E_3) corresponding to intra- and inter-laminar crack opening directions, respectively, also make a significant contribution to the calculated SIF. Measured SIFs increase as shear moduli and elastic moduli in the respective crack opening directions increase. Meanwhile, the resulting fluctuations in Poisson's ratios (υ_{12}, υ_{13}) have almost no effect on extracted SIFs. The reported Poisson's ratios are less accurate than the elastic and shear moduli calculated by this ultrasonic method (Eqs. (6) and (7)). That is, a 1% change in ultrasonic wave speed V_{66} (easily within the uncertainty of this method) results in a 32% change in υ_{12}, a 15% change in υ_{13}, and a 1% change in E_1. A similar 1% change in V_{11} results in a 2% change in E_1, a 0.03% change in E_2 and E_3, and a 2% change in υ_{12}. Thus for applications of this method to materials of high degree of anisotropy where the accuracy of the Poisson terms is essential, the authors recommend independent verification of the Poisson's ratios.

3.5. Finite element analysis

Finite element analyses were carried out to supplement dynamic experimental results prior to crack initiation. A 3-D, transient, elasto-dynamic, finite element model using ABAQUS®/Explicit software was developed. The numerical model

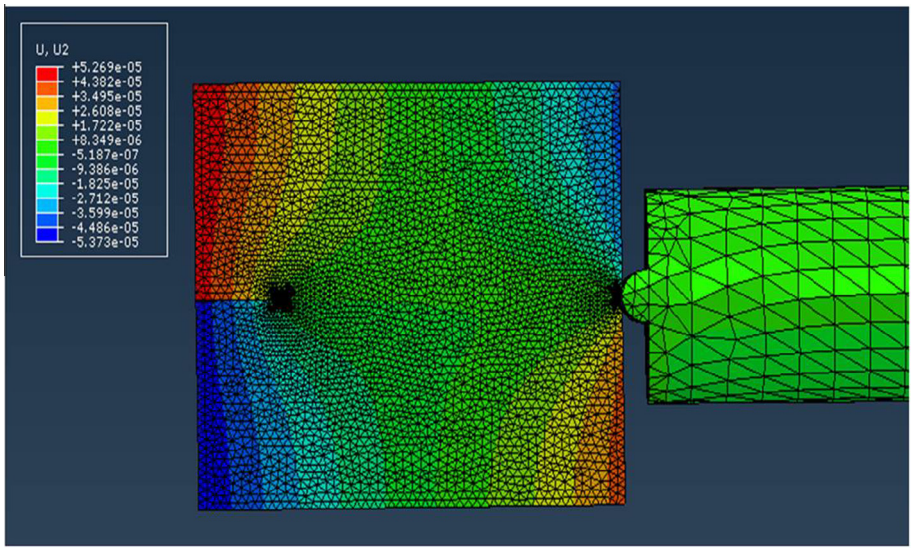

Fig. 11. Finite element model of a neat intralaminar specimen. Crack opening displacement contours correspond to a time instant 23 μs after impact and 1 μs before crack initiation.

included the specimen and the long-bar (Fig. 11) in order to ensure that the stress wave propagating into the specimen was captured as accurately as possible. Material property input for the model included all of the elastic properties in Table 3, along with the density. The model consisted of 218,000 tetrahedral elements with highly refined elements of size 0.1 mm in the impact and crack tip vicinities. The model had a total of 133,000 degrees of freedom. The particle velocity (V_{pI}) in the bar was determined from the measured strain history on the long-bar using Eq. (8)

$$V_{pI} = c_I \varepsilon_I \tag{8}$$

and input at the far right flat surface of the long-bar (Fig. 11). (In the above subscript I denotes 'incident,' c the bar wave speed and ε the measured strain on the long-bar.) After propagating along the long-bar (most of which is not pictured in Fig. 11), the stress waves were transmitted into the specimen using a contact definition for the semi-circular region that impacts the flat edge of the specimen. Time increments automatically chosen during computations by the software were approximately 5 ns.

Instantaneous values of SIFs were computed from finite element results using a regression analysis of crack flank displacements. Apparent stress intensity factors ($\bar{K}_I$) were calculated using crack opening displacements (δ_y) in Eq. (9) near the crack tip according to:

$$\delta_y|_{\theta=\pm\pi, r\to 0} = 2\overline{K}_I \sqrt{\frac{2r}{\pi}} \mathrm{Re}\left[\frac{1}{\mu_2 - \mu_1}(q_1\mu_2 z_1 - q_2\mu_1 z_2)\right]. \tag{9}$$

The linear regions of $\overline{K}_I$ versus r plots were then extrapolated to the crack tip to obtain instantaneous SIFs as $K_I = \lim_{r\to 0}\overline{K}$ [28,29].

4. Results

4.1. Quasi-static fracture results

To estimate baseline inter- and intra-laminar fracture parameters at crack initiation, quasi-static experiments were carried out on the 3-point bend configuration described in Section 3.1. Representative load–displacement curves are given for Neat (carbon fiber/epoxy without CNTs) samples in Fig. 12. Intralaminar specimens consistently showed more area under the curve than interlaminar specimens. Apart from the intrinsic inter- and

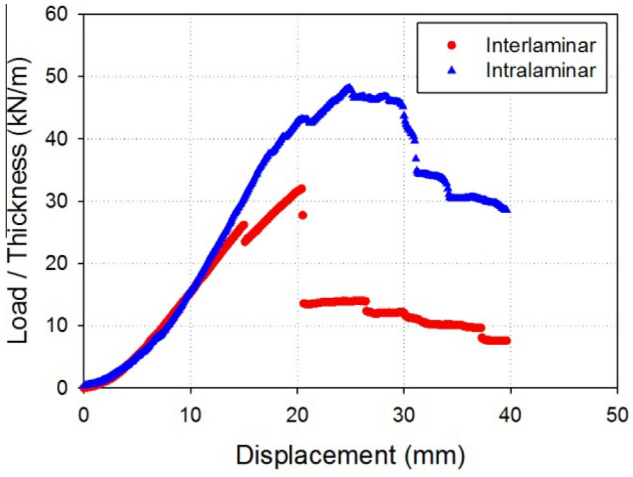

Fig. 12. Representative intralaminar and interlaminar load–displacement curves for Neat fracture specimens tested under quasi-static loading conditions.

intra-laminar elastic characteristics (Table 3), this increase is likely amplified by the presence of the thermoplastic-coated fiberglass scrim shown in Fig. 2 (initially believed by the authors to be an exclusively thermoplastic material). Thus, intralaminar cracks were aligned to propagate through the fiberglass scrim fibers, whereas interlaminar cracks propagated between layers of carbon fiber held by scrim without being affected by the scrim.

The measured SIF histories are shown in Fig. 13a and b from quasi-static fracture experiments for Neat samples (three experiments in each case to demonstrate repeatability) with cracks growing in the interlaminar and intralaminar directions, respectively. Intralaminar specimens had significantly higher critical SIFs than interlaminar specimens, likely attributed to the presence of the fiberglass scrim on each of the 60 layers of the original composite plates. Specimens exhibited controlled crack growth for several seconds after crack initiation (even longer for intralaminar specimens), and measured SIFs continued to increase due to fiber bridging [2]. The addition of CNTs (Fig. 13c and d) had no significant effect on quasi-static SIFs. The average quasi-static K_{IC} values at crack initiation are summarized in Fig. 14, where CNTs led to no improvement in K_{IC}, whereas the intralaminar specimens had

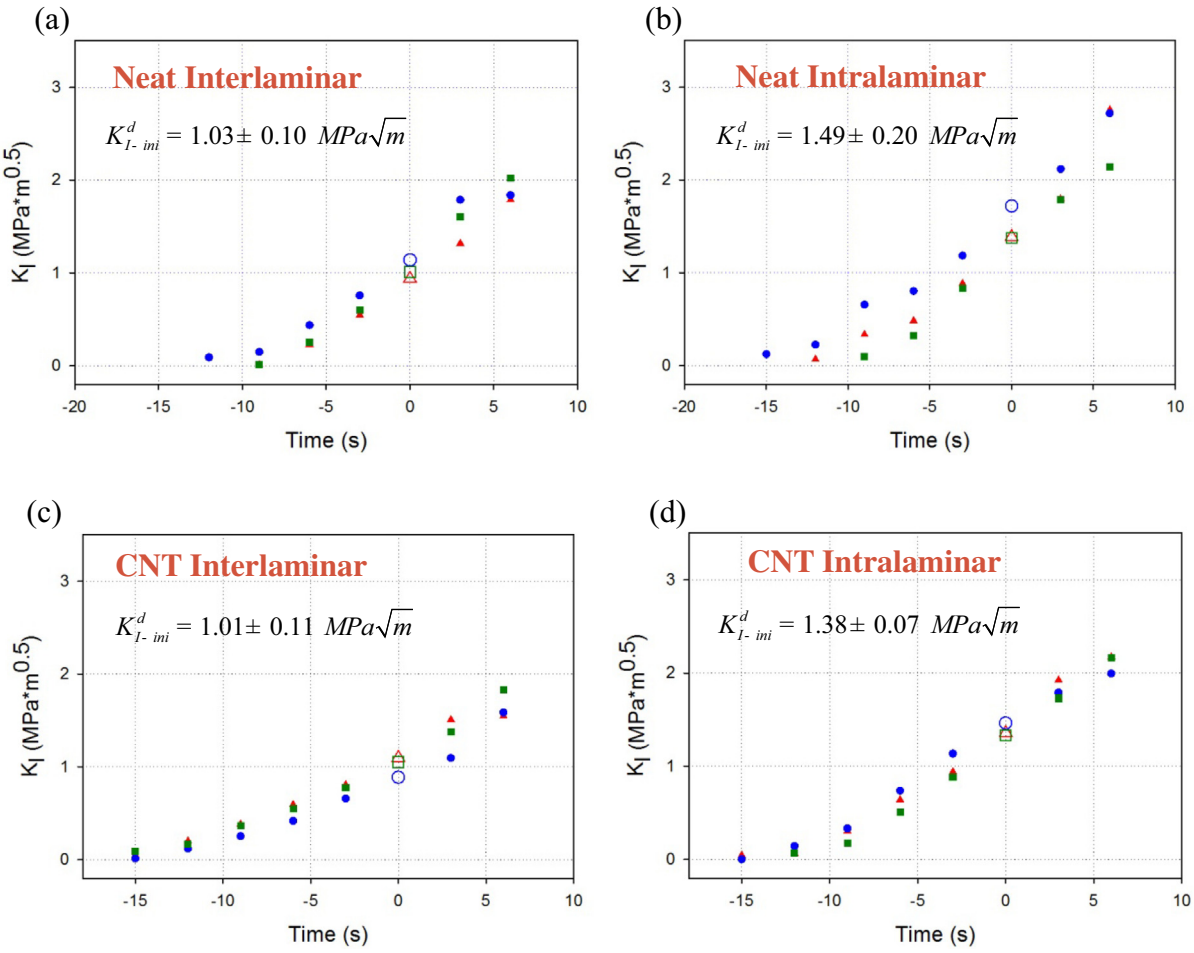

Fig. 13. Quasi-static SIF histories for edge-cracked specimens with cracks growing in the interlaminar or intralaminar directions. The open symbols denote crack initiation (designated by time $t = 0$).

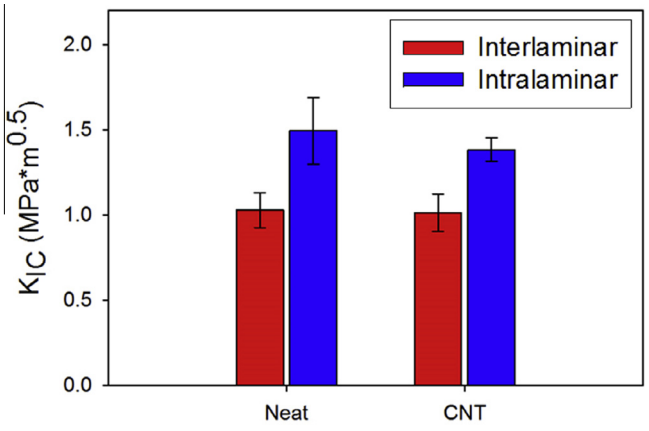

Fig. 14. Average of measured quasi-static K_{IC} values. Intralaminar specimens had significantly higher K_{IC} than interlaminar specimens, whereas the addition of CNTs did not have a significant effect on K_{IC}.

significantly higher K_{IC} values than the corresponding interlaminar specimens.

4.2. Dynamic fracture results

The measured SIF histories from dynamic fracture experiments are shown in Fig. 15a and b for Neat samples (three experiments in each case) with cracks growing in the interlaminar and intralaminar directions, respectively. As in the quasi-static case (Fig. 13), intralaminar specimens had significantly higher critical SIF (K^d_{I-ini}) and post-initiation SIFs (K^d_I) than interlaminar specimens, likely attributed to the presence of the thermoplastic-coated fiberglass scrim. The solid lines indicate FEA models (aligned with the average crack initiation SIF) generated using strain gage data on the long-bar which closely match the pre-initiation SIF values obtained from DIC and high speed photography. The addition of CNTs (Fig. 15c and d) gave similar K^d_{I-ini} and K^d_I values to corresponding Neat specimens, but with a higher degree of scatter. This increase in scatter was likely due to inconsistencies in dispersion of CNTs near the crack tip.

The measured crack tip velocity histories are given in Fig. 16. Following crack initiation, the intralaminar cracks quickly decelerated and eventually arrested, whereas the interlaminar cracks accelerated to 600–800 m/s. The intralaminar samples with CNTs had lower crack tip velocities than corresponding Neat specimens, indicating higher resistance to crack growth; however, these specimens also had reduced average K^d_{I-ini}. The average dynamic K^d_{I-ini} values are summarized in Fig. 17, where CNTs gave an insignificant reduction of K^d_{I-ini}, whereas the intralaminar specimens had significantly higher K^d_{I-ini} values than the corresponding interlaminar specimens. All quasi-static (QS) and dynamic (D) critical SIF values

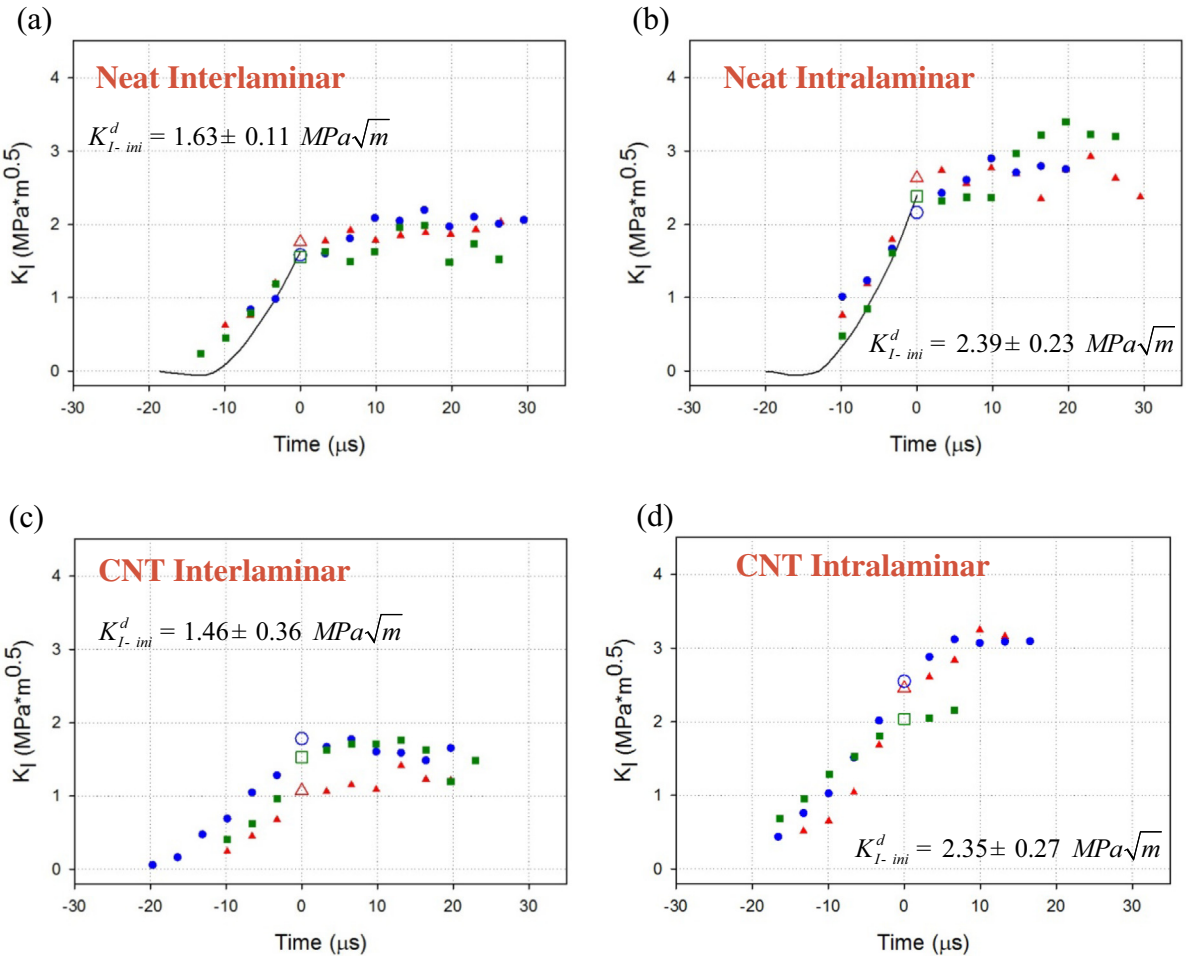

Fig. 15. Dynamic SIF histories for CFRP specimens with cracks growing in the interlaminar and intralaminar directions. Results from FEA are indicated by the solid line in (a) and (b). Open symbols denote values at crack initiation, at time $t = 0$.

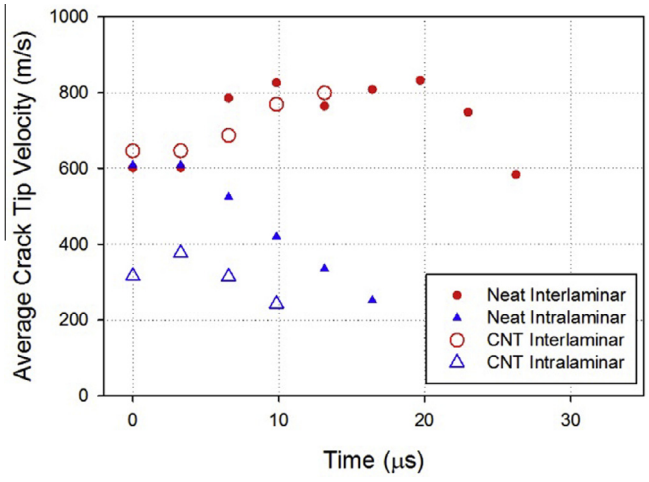

Fig. 16. Crack tip velocities of CFRPs. Following crack initiation, intralaminar cracks (blue) decelerated quickly and arrested, whereas interlaminar cracks (red) accelerated to ~800 m/s. (For interpretation of the references to colour in this figure legend, the reader is referred to the web version of this article.)

are listed in Table 4 along with the corresponding loading rate ($\dot{K}$), quantified by the rate of change of SIF immediately before crack initiation.

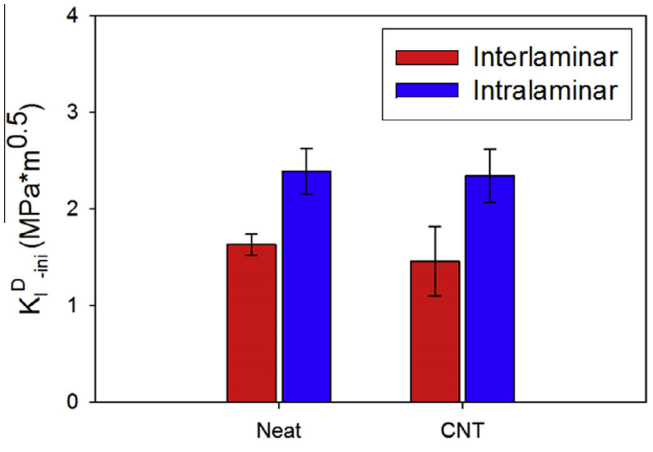

Fig. 17. Average of measured dynamic (K^d_{I-ini}) values. Intralaminar specimens had significantly higher (K^d_{I-ini}) than interlaminar specimens, whereas the addition of CNTs caused a slight reduction in (K^d_{I-ini}).

Because fracture toughness is typically reported in terms of G_{IC} instead of critical SIF in the composites community, K_{IC}/K^d_{I-ini} values have been converted to G_{IC}/G^d_{I-ini} in Table 5 using the following equation for intralaminar fracture [30]:

Table 4
Average quasi-static (QS) and dynamic (D) critical SIF values for interlaminar and intralaminar specimens.

Test type	Average rate $\dot{K}$ (MPa $\sqrt{m}$ s^{-1})	Average Neat K_{IC}/K^d_{I-ini} (MPa $\sqrt{m}$)	Average CNT K_{IC}/K^d_{I-ini} ($MPa\sqrt{m}$)
QS inter	1.31×10^{-1}	1.03 ± 0.10	1.01 ± 0.11
QS intra	1.76×10^{-1}	1.49 ± 0.20	1.38 ± 0.07
D inter	1.55×10^{5}	1.63 ± 0.11	1.46 ± 0.36
D intra	2.14×10^{5}	2.39 ± 0.23	2.35 ± 0.27

Table 5
Average fracture toughness G_{IC}/G^d_{I-ini} calculated from K_{IC}/K^d_{I-ini} values (QS = quasi-static and D = dynamic).

Test Type	Average Neat $G_{IC}/G^d_{I-ini}(J/m^2)$	Average CNT $G_{IC}/G^d_{I-ini}(J/m^2)$
QS inter	109 ± 22	149 ± 31
QS intra	197 ± 52	177 ± 17
D inter	274 ± 38	318 ± 146
D intra	500 ± 98	514 ± 115

$$G_I = -\frac{K_I^2}{2} S_{22} \mathrm{Im}\left[\frac{\mu_1 + \mu_2}{\mu_1 \mu_2}\right],$$

where $\mu_j (j = 1, 2)$ are the two roots of : $S_{11}\mu^4 + (2S_{12} + S_{66})\mu^2 + S_{22} = 0$ (10)

and the following equation for interlaminar fracture:

$$G_I = -\frac{K_I^2}{2} S_{33} \mathrm{Im}\left[\frac{\mu_1 + \mu_2}{\mu_1 \mu_2}\right],$$

where $\mu_j (j = 1, 2)$ are the two roots of : $S_{11}\mu^4 + (2S_{13} + S_{55})\mu^2 + S_{33} = 0$. (11)

the average fracture toughness values for quasi-static G_{IC} and dynamic G^d_{I-ini} are given in Fig. 18, converted from critical SIFs according to Eqs. (10) and (11). While CNTs did not lead to improvements in critical stress intensity factors, they produced a 34% insignificant improvement in quasi-static interlaminar G_{IC} and a 16% insignificant improvement in dynamic interlaminar G^d_{I-ini} over Neat interlaminar samples. CNT-infused nanocomposites had similar intralaminar fracture toughness compared to corresponding neat samples, where fracture was dominated by the fiberglass scrim.

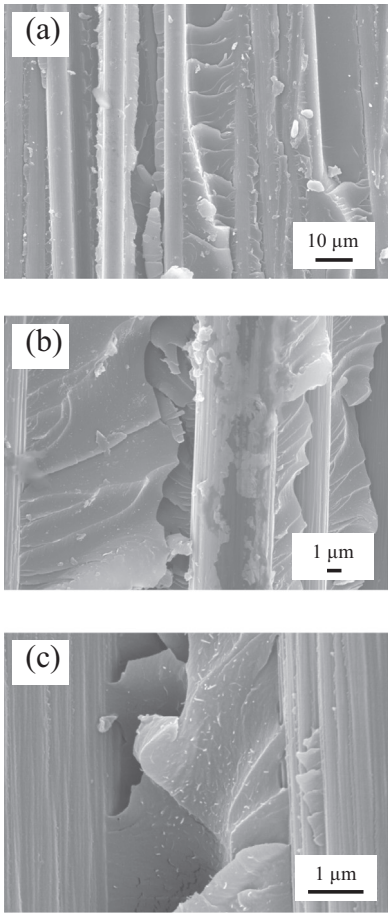

Fig. 19. Scanning electron microscopy of (a) Neat CFRP at 1000×, (b) CNT CFRP at 4000×, and (c) CNT CFRP at 15000×. Crack growth is in the vertical direction. CNTs appear to be reasonably well-dispersed throughout the resin layers, but have little effect on resin layer fracture features or measured critical SIF.

Scanning electron micrographs of Neat and CNT samples are shown in Fig. 19. Crack growth occurred along the fiber direction, vertically in each image. Addition of well-dispersed CNTs as evident in Fig. 19b and c does not appear to affect fracture surface features in the resin layer compared to the Neat fracture surface in Fig. 19a. This observation is consistent with the lack of critical SIF enhancements in the reported measurements.

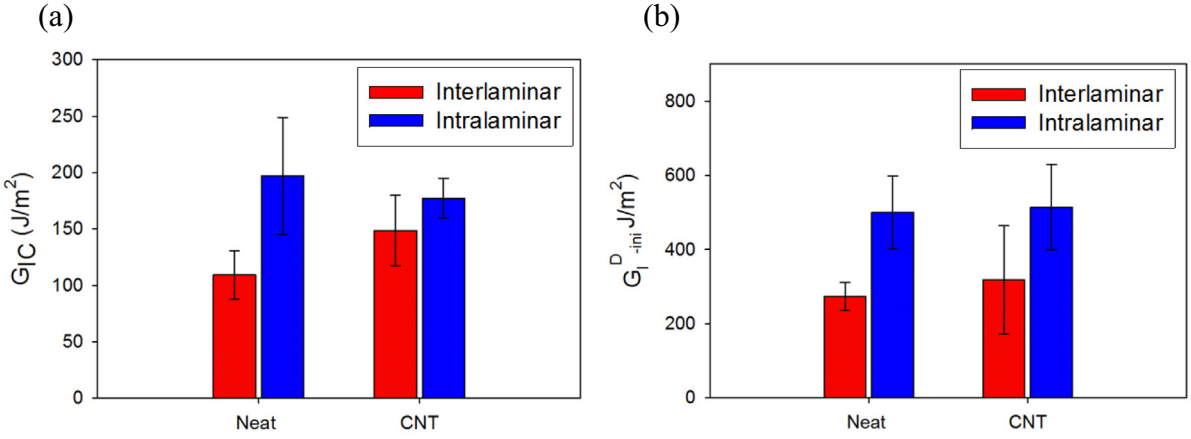

Fig. 18. Average fracture toughness values from critical SIFs using Eqs. (10) and (11) (a) quasi-static G_{IC} and (b) dynamic G^d_{I-ini} values. CNTs led to statistically insignificant improvements in both quasi-static (+34%) and dynamic (+16%) fracture toughness for interlaminar specimens, whereas intralaminar fracture of CNT-infused CFRPs, affected by fiberglass scrim, had similar fracture toughness compared to Neat samples.

5. Discussion and conclusions

In this study, all interlaminar fracture specimens have higher initiation SIF under dynamic conditions than under quasi-static conditions, although this perceived loading rate effect could be due to the framing rate used as detailed in Appendix B. The quasi-static G_{IC} values for interlaminar fracture toughness in Table B1 of Appendix B are in good agreement with the literature [2,11,14,16].

Despite the high quality of dispersion demonstrated in Fig. 19, the addition of CNTs did not improve the critical stress intensity factor (K_{IC}/K^{d}_{I-ini}), although improvement (+34%), comparable to those in the literature [8–16] in quasi-static interlaminar fracture toughness (G_{IC}) was found (Fig. 18). The errors are magnified in energy release rate calculations due to the squaring of the critical SIF in Eqs. (10) and (11), making improvements in fracture toughness statistically not significant. The scatter is particularly high for dynamic interlaminar fracture toughness of CNT-infused samples. Questions regarding scalability and cost-effectiveness of such preparations are not well documented at this time.

The volume fraction of fibers in the Neat CFRP processed for this work is on the lower end of the values reported in Tables 1 and 2 by other investigators. The addition of CNTs increased the viscosity of epoxy and caused a further reduction in V_f, which led to a slight reduction in critical stress intensity factor under both quasi-static (K_{IC}) and dynamic (K^{d}_{I-ini}) loading conditions. In the ideal case, three-phase nanocomposites should be compared with Neat epoxy/carbon fiber composites of the same V_f, although this variable is difficult to control due to the change in viscosity of the resin caused by well-dispersed CNTs.

The current work is unique in several respects:

(1) The fabrication of relatively thick CFRPs allows for the comparison of interlaminar and intralaminar fracture data using the same testing procedures with samples machined to the same dimensions from the same original block of material. Under quasi-static loading conditions, where all material points sense the imposed loads simultaneously, measured SIFs are dependent on specimen geometry [5–7]. Under stress wave loading conditions, on the other hand, measured SIFs are also dependent on elastic wave speeds, which differ significantly between interlaminar and intralaminar directions (Table 3). The presence of fiberglass scrim on the front and back surfaces of the unidirectional carbon fiber fabric pinned intralaminar cracks whereas interlaminar cracks propagated through unsupported epoxy resin at the interlayer. Future work to achieve this idealized comparison of interlaminar and intralaminar fracture could involve similar preparation of thick carbon fiber composites using either unidirectional prepreg or dry unidirectional fabric held together by a thermoplastic scrim.

(2) There is no current ASTM standard to study dynamic interlaminar fracture of composite materials. The current ASTM standard for quasi-static interlaminar fracture of composite materials (D5528) cannot be extended to study dynamic interlaminar fracture because thin specimens generally experience flexural stress waves. As the aerospace industry continues to replace aluminum with CFRP exposed to high speed events and cold temperatures, the behavior of these materials under dynamic loading conditions must be understood. Advantages of the current methodology involving DIC and high-speed photography include non-contact full-field deformations for the measurement of SIFs, as well as the precise location of the crack tip during the fracture event, which is necessary for estimating crack tip velocities for an accurate evaluation of dynamic SIF histories and hence crack growth resistance.

(3) While several researchers [18–20] have previously investigated dynamic interlaminar fracture of CFRPs, they have assumed transverse isotropy and relied on statically-measured elastic properties in order to estimate dynamic fracture properties. In addition, they appear to have each used elastic properties reported by others who used similar materials. In other instances, out-of-plane elastic characteristics are estimated based on in-plane measurements of the same. The current research, on the other hand, includes the ultrasonic estimation of all dynamic elastic properties for orthotropic CFRP materials machined from the same composite plate, producing a high degree of consistency and reliability when in-plane and out-of-plane fracture characteristics are compared.

Acknowledgment

This work was supported by a NASA Office of the Chief Technologist's Space Technology Research Fellowship (NSTRF #NNX11AM80H). Technical assistance of Geoffrey Thompson at Auburn University and Dr. James Ratcliffe at NASA Langley Research Center is greatly appreciated. Assistance of Drs. M. Hosur, A. Tcherbi-Narteh, Mr. M. Davis of Tuskegee University during processing of CNT-modified epoxy used in this work is also gratefully acknowledged. Special thanks to V2 Composites, Inc. and Momentive Specialty Chemicals, Inc. for providing unidirectional carbon fiber and epoxy, respectively, for this investigation.

Appendix A

In order to further verify the ultrasonic determination of elastic constants, the method was calibrated relative to data on bovine

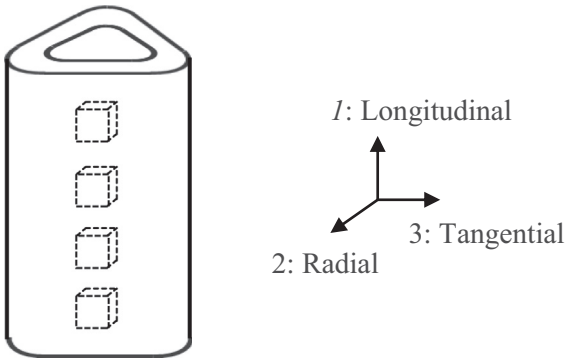

Fig. A1. Alignment of cortical bone ultrasonic specimens.

Table A1
Ultrasonically-determined elastic constants of dried cortical bone.

Material Property	Our Data	Literature[27]
$E_1 = E_L$ (GPa)	25.7	26.5
$E_2 = E_R$ (GPa)	20.6	18.1
$E_3 = E_T$ (GPa)	19.1	19.4
$G_{23} = G_{RT}$ (GPa)	8.17	7.22
$G_{13} = G_{LT}$ (GPa)	9.04	8.67
$G_{12} = G_{LR}$ (GPa)	9.49	8.65
$\nu_{12} = \nu_{LR}$	0.23	0.207
$\nu_{13} = \nu_{LT}$	0.32	0.305
$\nu_{23} = \nu_{RT}$	0.31	0.325
$\nu_{21} = \nu_{RL}$	0.18	0.283
$\nu_{31} = \nu_{TL}$	0.24	0.285
$\nu_{32} = \nu_{TR}$	0.29	0.222
ρ (kg/m^3)	2000	–

Table B1
Neat critical SIF assigned to the image before versus after crack initiation, reported in terms of K_{IC}/K^d_{I-ini} and G_{IC}/G^d_{I-ini} (QS = quasi-static and D = dynamic).

Test type	Neat before K_{IC}/K^d_{I-ini} (MPa $\sqrt{m}$)	Neat After K_{IC}/K^d_{I-ini} (MPa $\sqrt{m}$)	Neat before G_{IC}/G^d_{I-ini} (J/m^2)	Neat after G_{IC}/G^d_{I-ini} (J/m^2)
QS inter	1.03 ± 0.10	1.57 ± 0.24	109 ± 22	256 ± 75
QS intra	1.49 ± 0.20	1.90 ± 0.19	197 ± 52	316 ± 65
D inter	1.63 ± 0.11	1.67 ± 0.09	274 ± 38	285 ± 32
D intra	2.39 ± 0.23	2.49 ± 0.22	500 ± 98	544 ± 95

cortical bone available in the literature. The bovine cortical bone was dried and machined to cubes of ~6 mm side, with each face aligned with one of the three material directions (see Fig. A1). These samples were further machined to measure off-diagonal C-matrix coefficients as shown in Fig. 10. Ultrasonic results were successfully compared to those reported by Van Buskirk et al. [27] from a dried human femur (Table A1), further confirming the method used for fiber reinforced composites work.

Appendix B

Using the current methodology, critical SIF refers to the SIF value calculated from the last image before the crack was observed to move in the sequence of photographs. Alternatively, if the initiation SIF is chosen to be the first image when the crack is observed to move, the assigned quasi-static initiation SIF values increase significantly, whereas the assigned dynamic initiation SIF values increase only slightly. This is because quasi-static SIFs continue to increase at approximately the same rate before and after crack initiation (Fig. 13), whereas dynamic SIFs level off dramatically after initiation (Fig. 15), particularly in the interlaminar case where the scrim fibers do not participate in crack growth. Accordingly, Table B1 compares Neat K_{IC}/K^d_{I-ini} and G_{IC}/G^d_{I-ini} values calculated from the image before and after crack initiation.

In light of this, future works could use a slower loading rate or a faster framing rate, particularly under quasi-static conditions, in order to improve estimation of K_{IC} and G_{IC} values by this methodology.

References

[1] Cowley KD, Beaumont PWR. The interlaminar and intralaminar fracture toughness of carbon-fibre/polymer composites: the effect of temperature. Compos Sci Technol 1997;57:1433–44.
[2] Czabaj MW, Ratcliffe JG. Comparison of intralaminar and interlaminar mode I fracture toughnesses of a unidirectional IM7/8552 carbon/epoxy composite. Compos Sci Technol 2013;89:15–23.
[3] de Moura MFSF, Campilho RDSG, Amaro AM, Reis PNB. Interlaminar and intralaminar fracture characterization of composites under mode I loading. Compos Struct 2010;92:144–9.
[4] Truss RW, Hine PJ, Duckett RA. Interlaminar and intralaminar fracture toughness of uniaxial continuous and discontinuous carbon fibre epoxy composites. Compos A Appl Sci Manuf 1997;28:627–36.
[5] Sakai M, Kurita H. Size-effect on the fracture toughness and the R-curve of carbon materials. J Am Ceram Soc 1996;79:3177–84.
[6] Smith JA, Rolfe ST. The effect of crack depth (a) and crack depth to width ratio (A/W) on the fracture toughness of A533-B steel. J Press Vessel Technol Trans ASME 1994;116:115–21.
[7] Wang Z-X, Xue F, Lu J, Shi H-J, Shu G-G. Experimental and theoretical investigation of size effects on the ductile/brittle fracture toughness of a pressure steel. Int J Damage Mech 2010;19:611–29.
[8] Almuhammadi K, Alfano M, Yang Y, Lubineau G. Analysis of interlaminar fracture toughness and damage mechanisms in composite laminates reinforced with sprayed multi-walled carbon nanotubes. Mater Des 2014;53:921–7.
[9] Ashrafi B et al. Enhancement of mechanical performance of epoxy/carbon fiber laminate composites using single-walled carbon nanotubes. Compos Sci Technol 2011;71:1569–78.
[10] Godara A et al. Influence of carbon nanotube reinforcement on the processing and the mechanical behaviour of carbon fiber/epoxy composites. Carbon 2009;47:2914–23.
[11] Hu N et al. Reinforcement effects of MWCNT and VGCF in bulk composites and interlayer of CFRP laminates. Compos B Eng 2012;43:3–9.
[12] Joshi SC, Dikshit V. Enhancing interlaminar fracture characteristics of woven CFRP prepreg composites through CNT dispersion. J Compos Mater 2012;46:665–75.
[13] Karapappas P, Vavouliotis A, Tsotra P, Kostopoulos V, Paipetis A. Enhanced fracture properties of carbon reinforced composites by the addition of multi-wall carbon nanotubes. J Compos Mater 2009;43:977–85.
[14] Kim HS, Hahn HT. Graphite fiber composites interlayered with single-walled carbon nanotubes. J Compos Mater 2011;45:1109–20.
[15] Romhany G, Szebenyi G. Interlaminar crack propagation in MWCNT/fiber reinforced hybrid composites. Express Polym Lett 2009;3:145–51.
[16] Sager RJ et al. Interlaminar fracture toughness of woven fabric composite laminates with carbon nanotube/epoxy interleaf films. J Appl Polym Sci 2011;121:2394–405.
[17] Kumar P, Kishore NN. Initiation and propagation toughness of delamination crack under an impact load. J Mech Phys Solids 1998;46:1773–87.
[18] Sun CT, Han C. A method for testing interlaminar dynamic fracture toughness of polymeric composites. Compos B Eng 2004;35:647–55.
[19] Wosu SN, Hui D, Dutta PK. Dynamic mixed-mode I/II delamination fracture and energy release rate of unidirectional graphite/epoxy composites. Eng Fract Mech 2005;72:1531–58.
[20] Wu XF, Dzenis YA. Determination of dynamic delamination toughness of a graphite-fiber/epoxy composite using Hopkinson pressure bar. Polym Compos 2005;26:165–80.
[21] Lee D, Tippur HV, Jensen BJ, Bogert PB. Tensile and fracture characterization of PETI-5 and IM7/PETI-5 graphite/epoxy composites under quasi-static and dynamic loading conditions. J Eng Mater Technol Trans ASME 2011;133.
[22] R.W. Bedsole, C. Park, P.B. Bogert, H.V. Tippur, A critical evaluation of the enhancement of mechanical properties of epoxy modified using CNTs. Submitted for Publication.
[23] Sih GC, Paris PC, Irwin GR. On cracks in rectilinearly anisotropic bodies. Int J Fract Mech 1965;1:189–203.
[24] C. Liu, A.J. Rosakis, M.G. Stout, Dynamic fracture toughness of a unidirectional graphite/epoxy composite. In: Paper presented at the ASME international mechanical engineering congress and exposition. Proceedings of the symposium on "dynamic effects in composites structures". New York, NY; 2001 Nov 11–16.
[25] Castagnede B, Kim KY, Sachse W, Thompson MO. Determination of the elastic constants of anisotropic materials using laser generated ultrasonic signals. J Appl Phys 1991;70:150–7.
[26] Solodov I, Doering D, Busse G. Ultrasonic characterization of elastic anisotropy in composites: case study of CFRP. Mater Test Mater Compon Technol Appl 2008;50:602–8.
[27] Van Buskirk WC, Cowin SC, Ward RN. Ultrasonic measurement of orthotropic elastic constants of bovine femoral bone. J Biomech Eng Trans ASME 1981;103:67–72.
[28] Bedsole R, Tippur HV. Dynamic fracture characterization of small specimens: a study of loading rate effects on acrylic and acrylic bone cement. J Eng Mater Technol Trans ASME 2013;135.
[29] Rousseau CE, Tippur HV. Influence of elastic gradient profiles on dynamically loaded functionally graded materials: cracks along the gradient. Int J Solids Struct 2001;38:7839–56.
[30] Sun CT, Jin Z. Fracture mechanics. Waltham, MA: Academic Press; 2012.